Chapter IV:
MACHINE LEARNING IN SOLAR PHYSICS

https://doi.org/10.1017/S1743921322004847 Published online by Cambridge University Press

Yong-Jae Moon from Kyung Hee University (Republic of Korea) delivering the review talk on current applications of machine learning in heliospheric studies.

https://doi.org/10.1017/S1743921322004847 Published online by Cambridge University Press

The Era of Multi-Messenger Solar Physics
Proceedings IAU Symposium No. 372, 2023
G. Cauzzi & A. Tritschler, eds.
doi:10.1017/S1743921322004847

Application of Deep Learning to Solar and Space Weather Data

Yong-Jae Moon[1,2], Harim Lee[2], Jihyeon Son[1], Suk-Kyung Sung[2], Kangwoo Yi[2], Hyun-Jin Jeong[1], Eunsu Park[3], Eun-Young Ji[2], Il-Hyun Cho[2], Bendict Lawrance[2], Daye Lim[4], Gyungin Shin[5], Sujin Lee[6], Sumiaya Rahman[1] and Taeyoung Kim[1,7]

[1]School of Space Research, Kyung Hee University, Yongin, 17104, Republic of Korea

[2]Department of Astronomy and Space Science, College of Applied Science, Kyung Hee University, Yongin, 17104, Republic of Korea

[3]Korea Astronomy and Space Science Institute, Daejeon, 34055, Republic of Korea

[4]Centre for mathematical Plasma-Astrophysics, Department of Mathematics, KU Leuven Leuven, 3001, Belgium

[5]Department of Engineering Science, University of Oxford, Oxford, United Kingdom

[6] Space Center, Republic of Korea Air Force, Gyeryong, Republic of Korea

[7]AI Factory, Daejeon, Republic of Korea

Abstract. In this review, we introduce our recent applications of deep learning to solar and space weather data. We have successfully applied novel deep learning methods to the following applications: (1) generation of solar farside/backside magnetograms and global field extrapolation based on them, (2) generation of solar UV/EUV images from other UV/EUV images and magnetograms, (3) denoising solar magnetograms using supervised learning, (4) generation of UV/EUV images and magnetograms from Galileo sunspot drawings, (5) improvement of global IRI TEC maps using IGS TEC ones, (6) one-day forecasting of global TEC maps through image translation, (7) generation of high-resolution magnetograms from Ca II K images, (8) super-resolution of solar magnetograms, (9) flare classification by CNN and visual explanation by attribution methods, and (10) forecasting GOES solar X-ray profiles. We present major results and discuss them. We also present future plans for integrated space weather models based on deep learning.

Keywords. THE SUN, Sun: general, Sun: magnetic fields, methods: data analysis, techniques: image processing

1. Introduction

Deep learning (DL), which has been developed to find the best mathematical manipulation to turn the input into the output, is being applied to various fields and producing tremendous results. The technology has also been applied to astronomy and space science in recent years, helping research such as unprecedented data generation, damaged/lost data recovery, data quality improvement, event classification, detection, and development of space weather forecasting models.

A DL model for image-to-image translation generates different types of data from one or several input data. The Pix2Pix (Isola et al. 2017) model based on the conditional Generative Adversarial Networks (cGAN; Mirza & Osindero 2014) was suggested for

the general purpose of image translation. In this review we apply this method for the generation of modern satellite data from distant past drawings, filling the data gap due to ground observation restrictions, removing noise, and converting a low-resolution image to a high-resolution image, generating the ionospheric Total Electron Content (TEC) map, 1-day forecasting of global TEC, etc. It is noted that there are several limitations such as artifacts found in high-resolution images by the Pix2Pix model. In this study, we have employed the image-to-image translation method (Pix2PixHD; Wang et al. 2018) for high-resolution images above 1 K. For scientific data applications, we develop a new image translation model, (Pix2PixCC; Jeong et al. 2022), with the inspector controlled by the correlation coefficient between the AI-generated image and the target image.

The Long Short-Term Memory (LSTM; Hochreiter & Schmidhuber 1997) is suitable for dealing with time-dependent data. Since the DL model, which has good performance in formalized data processing, was insufficient to solve problems with frequently changing I/O data, Sutskever et al. (2014) proposed a Sequence to Sequence (Seq2Seq) model based on LSTM using a general end-to-end approach to sequence learning with minimal assumptions about sequence structures. In this study, we predict the solar flare X-ray flux profile by designing the model to perform Seq2Seq frameworks using LSTM and attention mechanism.

Convolution Neural Networks (CNN), which are in the spotlight in image processing and computer vision, have already surpassed humans in their ability to classify and detect features many years ago. The excellent performance of CNN has been applied to develop space weather forecasting models such as the forecast of solar flare occurrence using full-disk solar magnetograms.

As artificial intelligence began to produce outstanding results, humans attempted to interpret the process of performing tasks inside the DL model. For CNN, a visual explanation such as guided backpropagation (Springenberg et al. 2014) and Gradient weighted Class Activation Mapping (Grad-CAM; Selvaraju et al. 2017) is possible. Here we develop a new DL flare forecasting model based on CNN to visually show where the important weights are distributed and compare them with the physical parameters of active regions.

In this review, we introduce various research results using novel DL methods conducted in the Sun and Space Weather Laboratory (SSWL) at Kyung Hee University (KHU). Section 2 introduces the studies using the image-to-image translation method, and Section 3 introduces space weather applications based on DL. A brief conclusion and prospects are given in section 4.

2. Image-to-Image Translation by Deep Learning

2.1. *Solar EUV images from magnetograms*

We apply novel DL methods to the image-to-image translation from solar magnetograms to solar ultraviolet (UV) and extreme UV (EUV) images (Park et al. 2019). For this, we consider two convolutional neural network models with different loss functions: one (Model A) is with L1 loss (L1), and the other (Model B) is with L1 and cGAN loss (LcGAN). We train the models using pairs of Solar Dynamics Observatory (SDO; Pesnell et al. 2012)/Atmospheric Imaging Assembly (AIA; Lemen et al. 2012) nine-passband (94, 131, 171, 193, 211, 304, 335, 1600, and 1700 Å) UV/EUV images and their corresponding SDO/Helioseismic and Magnetic Imager (HMI; Schou et al. 2012) magnetograms from 2011 to 2016. The models are evaluated by comparing pairs of SDO/AIA images and the corresponding ones generated in 2017. Our major results from this study are as follows. First, the models successfully generate solar UV and EUV images from SDO/HMI magnetograms (Figure 1). Second, the results from Model A are

https://doi.org/10.1017/S1743921322004847 Published online by Cambridge University Press

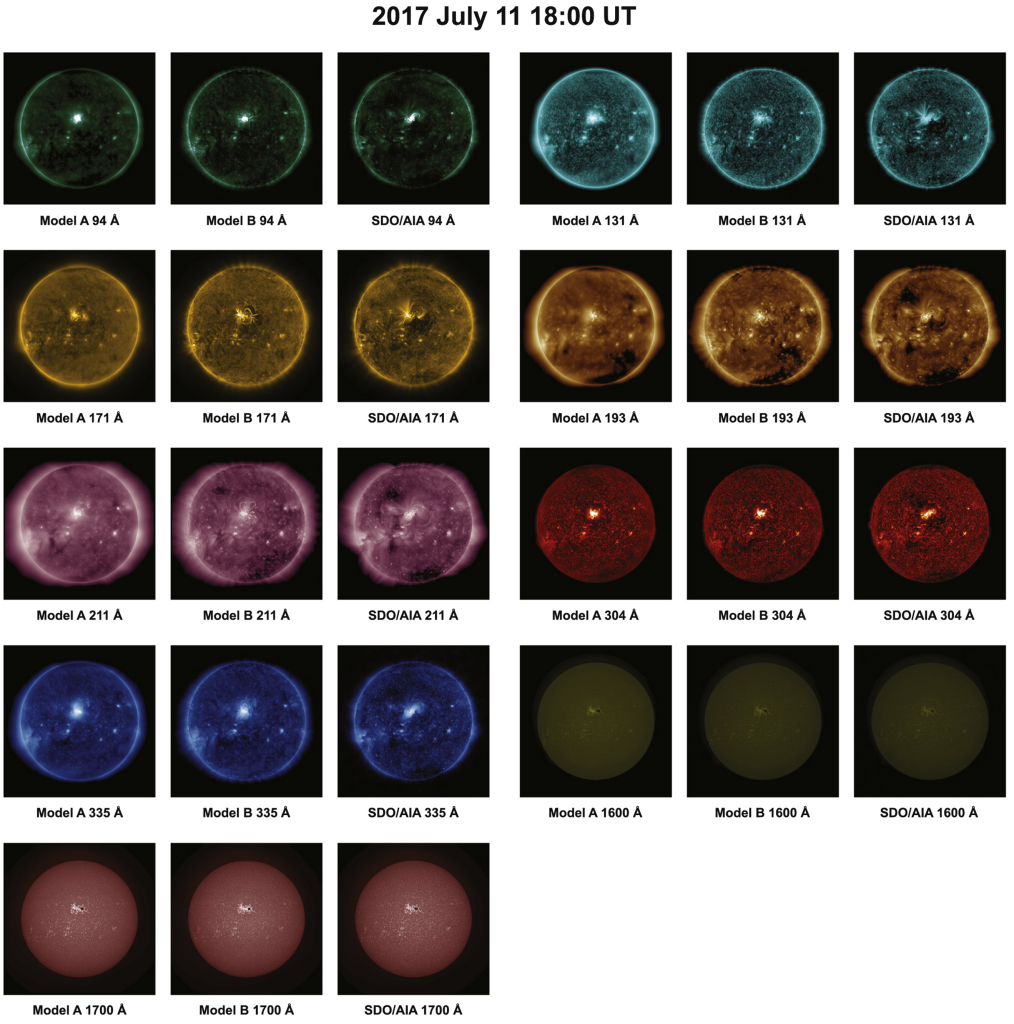

Figure 1. Comparison of real SDO/AIA images and the generated ones for nine passbands images at 12:00 UT on 2017 July 11. The first column shows generated images by Model A, the second column, the generated images by Model B, and the third column, SDO/AIA images (adapted from Park et al. (2018)).

slightly better than those from Model B in view of three metrics (pixel-to-pixel correlation coefficient (CC), relative error, and the percentage of pixels having errors less than 10 %). Third, in view of the RMS contrast measure, the generated images by Model A are much more blurred, which is due to the characteristics of convolution, than those by Model B because LcGAN is specialized for generating realistic images.

2.2. *Solar UV/EUV images from other UV/EUV images*

We use the above successful method on SDO/AIA 9 UV/EUV channels to find out which channel (or combination of channels) generated the most realistic image (Lim et al. 2021). 170 DL models with single-channel output (72 single-channel input models, 56 dual-channel input models, and 42 triple-channel input models) were developed and we evaluated the models with the pixel-to-pixel CC for the solar disk. Among the single-channel input models, the model with 131Å, among the dual-channel input models, the

https://doi.org/10.1017/S1743921322004847 Published online by Cambridge University Press

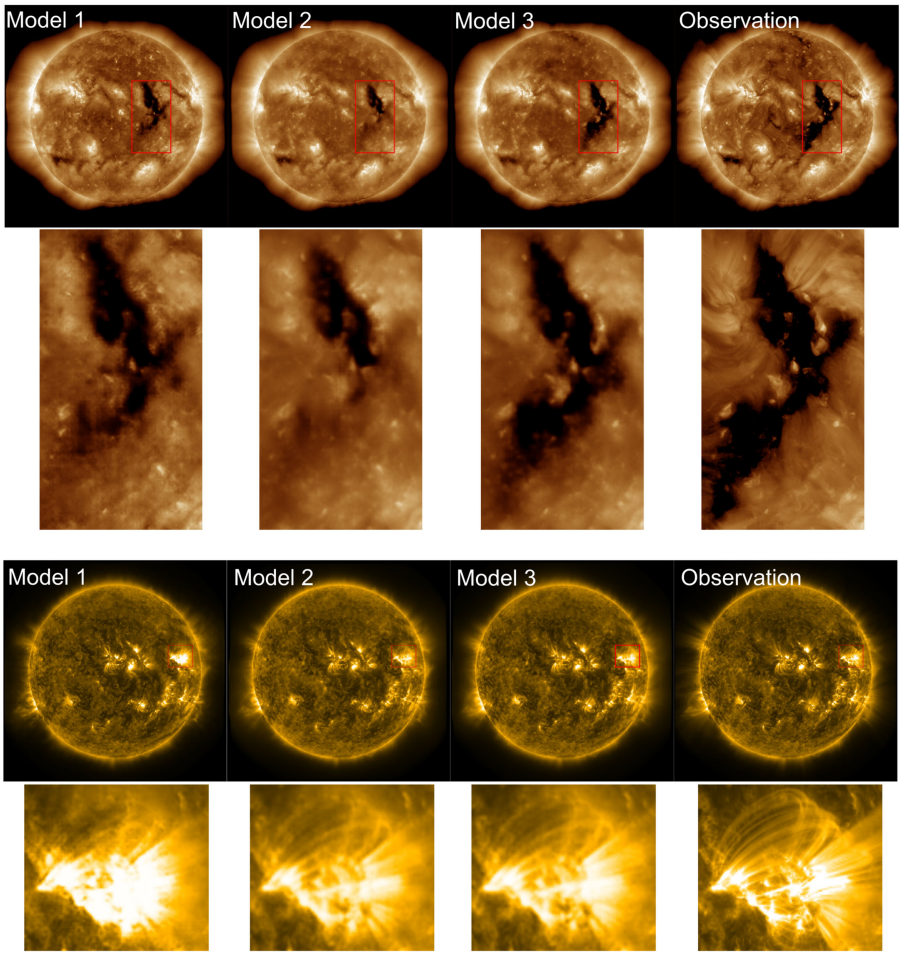

Figure 2. Comparison images between real and three model (Model 1: single-channel; Model 2: dual-channel; Model 3: triple-channel) results for CH and AR. The first and third rows are full disk images of 193Å and 171Å with CH and AR. The second and fourth rows show the regions (red boxes) magnified in the row above. The pixel-to-pixel CCs obtained from the three models are 0.92, 0.92, and 0.96 for CH, and 0.89, 0.96, and 0.97 for AR, respectively (adapted from Lim et al. (2021)).

model with 131Å and 1600Å, and among the triple-channel input models, the model with 131Å, 1600Å and 304Å have the highest average CC of 0.84, 0.95, and 0.97, respectively. The three passbands of the triple-channel model with the best performance are the channels that observe the coronal, upper photospheric, and chromospheric regions, respectively (Figure 2). This result may be taken into account when selecting channels for UV/EUV imaging instruments on solar satellites.

2.3. *Farside solar magnetograms from EUV images*

Magnetograms are significant for studying solar activity and predicting space weather disturbances. Farside/backside magnetograms can be constructed from local helioseismology without any farside data, but their quality is quite lower than that of typical frontside magnetograms. We generate farside solar magnetograms from Solar Terrestrial Relations Observatory (STEREO; Kaiser et al. 2008)/EUV 304 Å images using a DL

https://doi.org/10.1017/S1743921322004847 Published online by Cambridge University Press

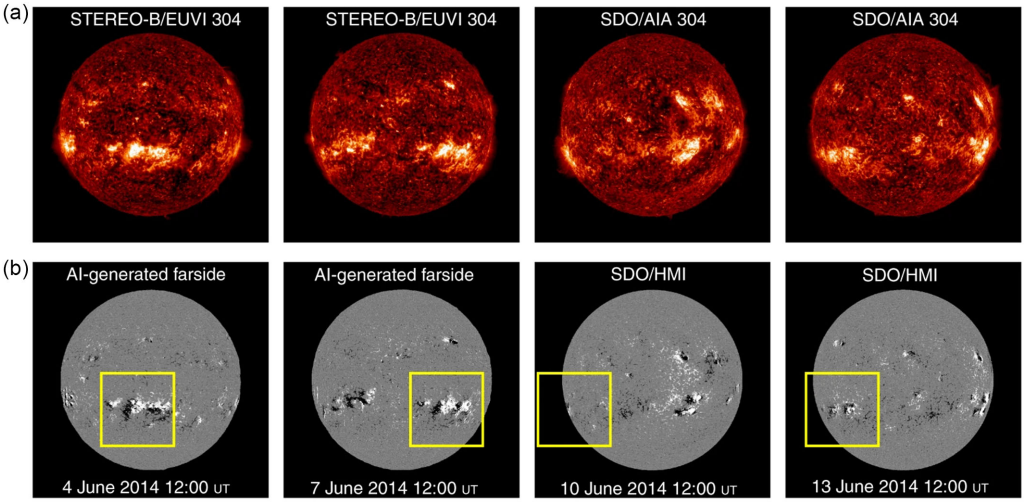

Figure 3. A series of 304Å images and magnetograms: a) the first two 304Å images are taken from STEREO-B/EUVI and the last two from SDO/AIA; b) the first two magnetograms are AI-generated farside ones from the model and the last two are SDO/HMI. The yellow boxes indicates the tracking of the NOAA active region 12087 from the farside to the frontside. We use ±100 G as the saturation level for both SDO/HMI and AI-generated magnetograms (adapted from Kim et al. (2019)).

model based on cGANs (Kim et al. 2019; hereafter KPL19). We train the model (Artificial Intelligence Solar Farside Magnetogram; AISFM v1.0) using pairs of SDO/AIA 304 Å images and SDO/HMI magnetograms taken from 2011 to 2017 except for September and October each year. The model is evaluated by comparing both SDO/HMI magnetograms and cGAN-generated magnetograms in September and October. Our method successfully generates frontside/backside solar magnetograms from SDO/AIA 304 Å images, and these are similar to those of the SDO/HMI. Thus we are able to monitor the temporal evolution of solar active regions from the farside to the frontside of the Sun using SDO/HMI (Figure 3) and farside magnetograms generated by our model when the farside EUV data are available.

Global magnetic fields of the solar corona are typically extrapolated from photospheric field data, for which farside data are taken when the AR was at the frontside, about two weeks earlier. For the first time, we construct the extrapolations of global magnetic fields using frontside and AI-generated farside magnetograms on a near-real time basis (Jeong et al. 2020). We generate the farside magnetograms from three channel images of STEREO Ahead (A) and Behind (B) by our DL model (AISFM v2.0) trained with frontside SDO EUV images and magnetograms. For frontside testing data sets, we demonstrate that the generated magnetic field distributions are quite consistent with the real ones; ARs as well as quiet regions (Figure 4). We make global magnetic field synchronic maps in which conventional farside data, which were taken many days ago, are replaced by farside ones generated by our model. The synchronic maps well produce not only the appearance of ARs but also the disappearance of others on the solar surface, which are much better than the conventional synoptic maps. We use these synchronized magnetic data to extrapolate the global coronal fields using the Potential Field Source Surface (PFSS) model. Our results are much more consistent with coronal EUV observations than those of the conventional method in view of solar active regions and coronal holes (Figure 5).

https://doi.org/10.1017/S1743921322004847 Published online by Cambridge University Press

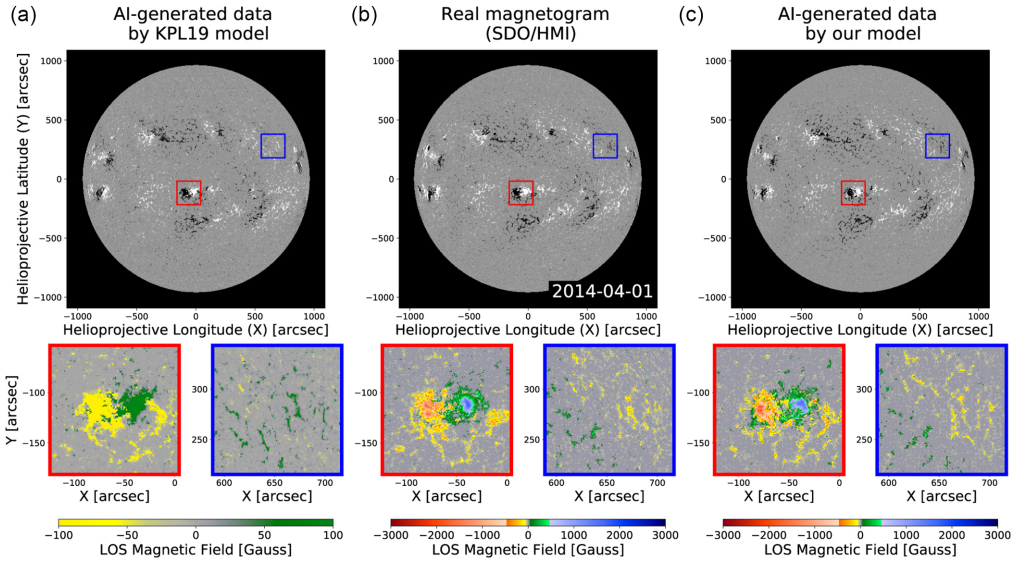

Figure 4. Comparisons of a real SDO/HMI magnetogram and AI-generated one: (a) AI-generated data by KPL19 model; (b) Real magnetogram on 2014 April 1 at 12:00 UT; (c) AI-generated one by the model. Full-disk magnetograms are displayed as white for positive polarity and black for negative one. A solar AR at disk center (red box) and a QR on the limb (blue box) are zoomed and represented with other color maps showing the large dynamic range values in Gauss (adapted from Jeong et al. (2020)).

We greatly improve AI-generated solar farside magnetograms using data sets from the STEREO and SDO (Jeong et al. 2020). We upgrade our previous DL model and input data sets to generate more realistic magnetograms than before. First, our model (AISFM v3.0), which is called Pix2PixCC (Figure 6), uses updated objective functions, which include CCs between the real and generated data. Second, we construct input data sets of our model: solar farside STEREO EUV images together with nearest frontside SDO data pairs of EUV ones and magnetograms. We expect that the frontside image pairs provide historic information on the distribution of magnetic field polarities. We demonstrate that magnetic field distributions generated by our model are much more consistent with the real ones than before, in view of several metrics. The averaged pixel-to-pixel CC for full disk, active regions, and quiet regions between real and AI-generated magnetograms with 8×8 binning are 0.88, 0.91, and 0.70, respectively. Total unsigned magnetic fluxes and net magnetic fluxes of the AI-generated magnetograms are consistent with those of real ones for the test data sets. It is interesting to note that our farside/backside magnetograms produce polar field strengths and magnetic field polarities consistent with those of nearby frontside magnetograms for solar cycles 24 and 25. Now we can monitor the temporal evolution of active regions using solar farside/backside magnetograms by the model together with the frontside ones. Our AI-generated solar farside magnetograms are now publicly available at the Korean Data Center for SDO (`http://sdo.kasi.re.kr`).

2.4. *Solar magnetograms and EUV images from sunspot drawings*

We generate solar magnetograms and EUV images from Galileo sunspot drawings using a DL model based on cGANs (Lee et al. 2021). We train the model using pairs of sunspot drawings from the Mount Wilson Observatory and their corresponding magnetograms (or EUV images) from 2011 to 2015 except for every June and December by

https://doi.org/10.1017/S1743921322004847 Published online by Cambridge University Press

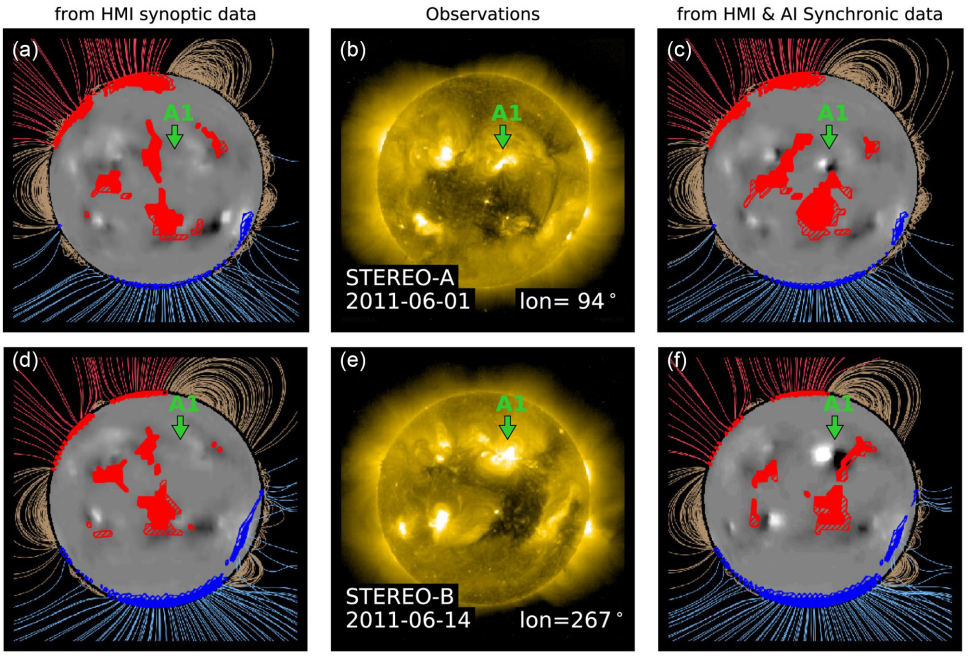

Figure 5. Comparisons of EUV observations and PFSS extrapolations from conventional and HMI and AI synchronic data (by our model) in full-disk observations. (a)-(c) Result of PFSS extrapolation from HMI synoptic data, EUV 284Å images, and PFSS extrapolations from SDO/HMI and AI synchronic data at the position of STEREO A on 2011 June 1. (d)-(f) Those at the position of STEREO-B on 2011 June 14. Positive and negative polarities of the open fields are displayed with blue and red colors. Closed field lines are indicated with dark yellow. Field lines at the limb and open field area on the surface are only shown for comparison. The PFSS is computed with source surface at $2.0R_{\odot}$ and $2.5R_{\odot}$, and those open field areas are displayed with hatched pattern and filled area, respectively. The solar surface is filled with the bottom boundary data to show the distribution of ARs. The green arrow indicates the appearance of the NOAA AR 11236 (adapted from Jeong et al. (2022)).

the Solar Dynamic Observatory satellite. We evaluate the model by comparing pairs of actual magnetograms (or EUV images) and the corresponding AI-generated image pairs in June and December. Our results show that bipolar structures of the AI-generated magnetograms are consistent with the original ones and their unsigned magnetic fluxes (or intensities) are consistent with the original ones. Applying this model to the Galileo sunspot drawings in 1612 (Galilei et al. 1613), we generate HMI-like magnetograms and AIA-like EUV images of the sunspots (Figure 7). We hope that the EUV intensities can be used for estimating solar EUV irradiance at long historical times. This study was publically introduced by AAS NOVA and Astronomy magazine.

2.5. *Solar magnetograms from Ca II images*

We generate realistic high-resolution (1024×1024 pixels) pseudo-magnetograms from Ca II K images using a DL model based on conditional generative adversarial networks (Shin et al. 2020). We consider a model "Pix2PixHD" that is specifically devised for high-resolution image translation tasks. We use Ca II K 393.3 nm images from the Precision Solar Photometric Telescope at the Rome Observatory (Ermolli et al. 1998, 2007) and magnetograms from the HMI at the SDO from 2011 January to 2015 June. 2465 pairs of Ca II K and HMI are used for training except for January and July data. The remaining

https://doi.org/10.1017/S1743921322004847 Published online by Cambridge University Press

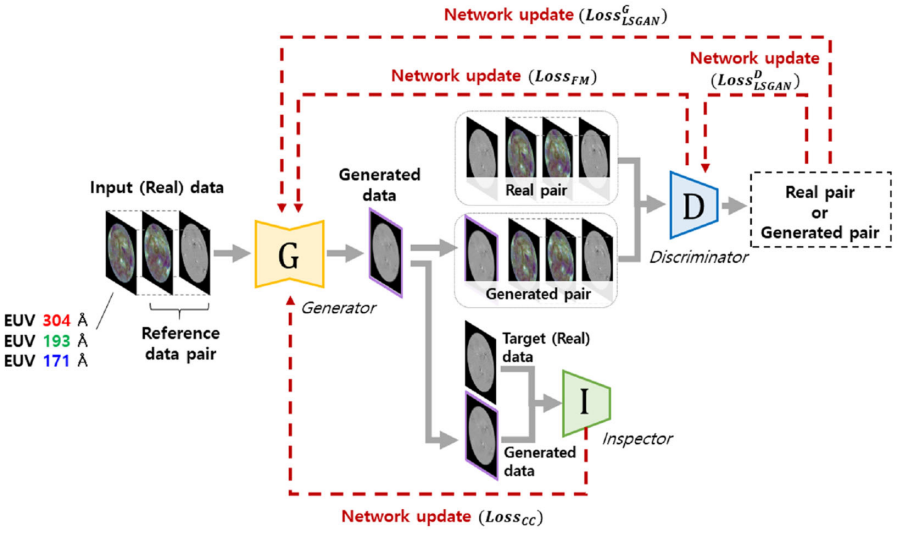

Figure 6. Flowchart and structures of the Pix2PixCC model. G, D, and I are the generator, discriminator, and inspector, respectively. The generator produces target-like data from input data. When we train the model, input data are SDO/AIA EUV 304, 193, and 171 Å images and a reference data pair. The reference data pair is composed of the three SDO EUV images and the corresponding SDO/HMI magnetogram, which are taken at the nearest available time. The discriminator trains for distinguishing between the real pair and generated ones. The real pair is composed of input data and target data, and the generated pair consists of input data and generated data. The inspector computes CCs between the target data and generated data. The generator and discriminator are updated by the losses calculated from the inspector and discriminator (adapted from Jeong et al. (2022)).

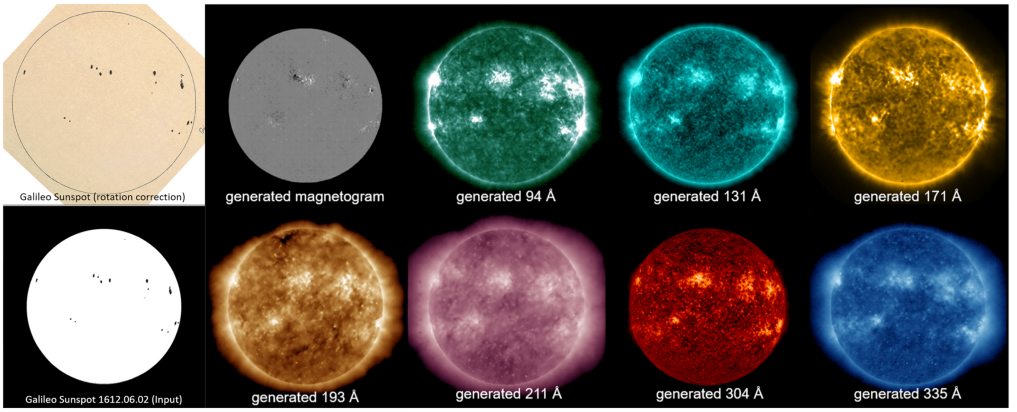

Figure 7. Results of our model when the Galileo sunspot drawings are used for input data: AI-generated magnetogram and UV/EUV images from the Galileo sunspot drawing on 1612 June 2 (modified from Lee et al. (2021a)).

436 pairs are used for an evaluation of the model. Our model shows that the average CC of total unsigned magnetic flux between AI-generated and real ones is 0.99 and the mean pixel-to-pixel CC after 8×8 binning over the full disk is 0.74. We find that the AI-generated absolute magnetic flux densities are very consistent with real ones, even in the fine-scale structures of quiet regions (Figure 8). On the other hand, the average pixel-to-pixel correlations of magnetic flux densities strongly depend on a region of interest: 0.81

https://doi.org/10.1017/S1743921322004847 Published online by Cambridge University Press

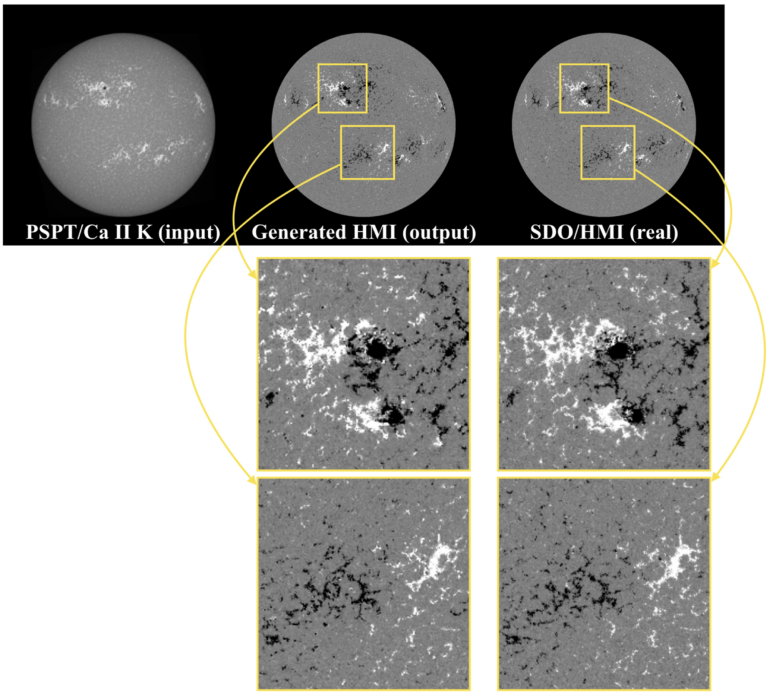

Figure 8. (Upper left) a Ca II K input intensity image, (upper middle) a generated HMI-like magnetogram, and (upper right) the corresponding real SDO/HMI. Ca II K and real SDO/HMI are taken at 18:48 UT 2012 January 31. (Lower left column) enlarged views of active regions in the generated magnetogram. (Lower right column) those in the real magnetogram. The white area represents positive polarities and the black area represents negative ones. For visual purpose, magnetic flux densities are expressed within ±100 G (adapted from Shin et al. (2020)).

for active regions and 0.24 for quiet regions. Our results suggest a sufficient possibility that we can produce high-resolution solar magnetograms from historical Ca II data.

2.6. *Solar He I 1083 nm images from EUV images*

We generate He I 1083 nm images from SDO/AIA images using a Pix2PixHD model based on cGAN (Son et al. 2021). He I 1083 nm images, the target data, were obtained from National Solar Observatory (NSO)/Synoptic Optical Long-term Investigations of the Sun (SOLIS; Keller et al. 2003). We make three DL models: single-input SDO/AIA 19.3 nm image for Model I, single-input 30.4 nm image for Model II, and double-input (19.3 and 30.4 nm) images for Model III. We use the data from 2010 October to 2015 July except for June and December for training and the remaining one for test. Major results of our study are as follows. First, the models successfully generate He I 1083 nm images with good correlations. Second, Model III has better results than those with single input image in view of metrics such as root mean square error (RMSE) and correlation coefficient (CC). RMSE and CC between real and synthetic ones for model III after 4 by 4 binnings are 9.49 and 0.88, respectively. Third, the AI-generated images show well observational structures such as active regions, filaments, and coronal holes. By our model, He I 1083 nm images can be generated with high time resolutions without data gaps (Figure 9), which would be useful for studying the time evolution of solar activity shown in He I 1083 nm observations.

https://doi.org/10.1017/S1743921322004847 Published online by Cambridge University Press

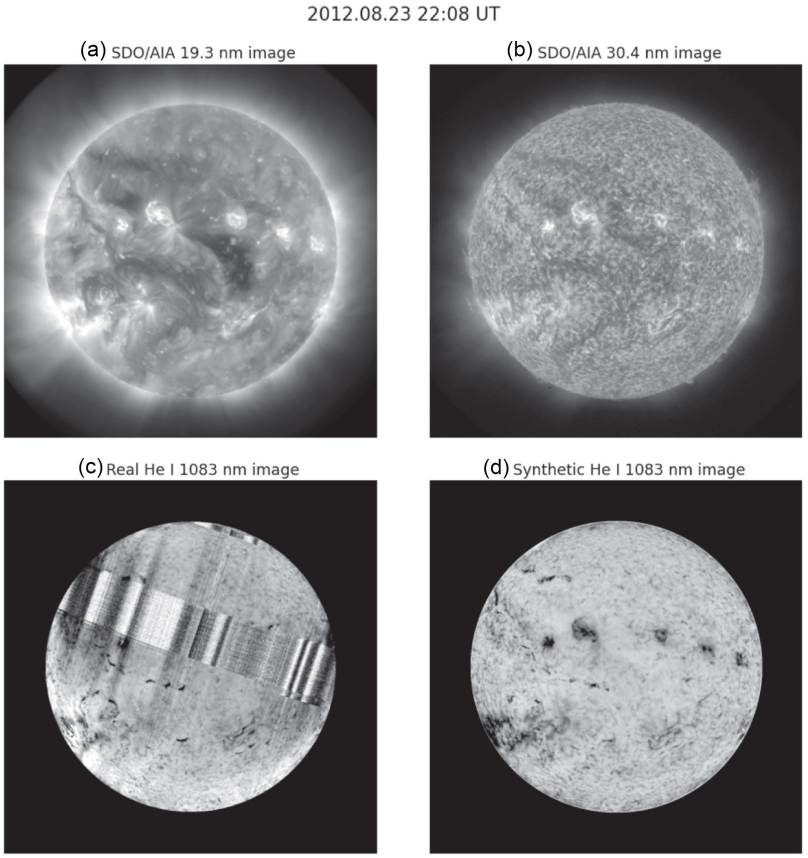

Figure 9. Restoration of damaged He I 1083 nm data at 22:08 UT on 2012 August 23 by our model: (a) SDO/AIA 19.3 nm image as input; (b) SDO/AIA 30.4 nm image as input; (c) observed He I 1083 nm image; (d) synthetic image from Model III (adapted from Son et al. (2021)).

2.7. *Solar coronal white-light images from EUV images*

The off-limb coronal white light images with an altitude range between 1.11 – 1.25 solar radii were generated from a single EUV channel image as well as multiple channel images by applying the DL model based on the cGANs (Lawrance et al. 2022). It was found that the AI-generated white light image shows the best correlation with the original K-Cor (de Wijn et al. 2012) image when multiple channels of the AIA 193 Å and 211 Å were used as input. The majority of low coronal structures such as helmet streamers, pseudostreamers, and polar coronal holes are well identified in the AI-generated ones as in the original images. It was also found that the positions and sizes of the polar coronal holes in the AI-generated images are well consistent with those of the original ones (Figure 10). In addition, the coronal mass ejections and jets were also well identified in the AI-generated images. Hence, the translation model from EUV images to white light images using the cGANs can provide complementary data to study the off-limb low coronal features in the white light when no ground-based observation is available due to the repeated night time, poor atmospheric conditions, and instrumental maintenance.

2.8. *Denoising solar magnetograms*

In astronomy, long-exposure observations are one of the important ways to improve signal-to-noise ratios (S/Ns). We apply a deep-learning model to de-noise solar

https://doi.org/10.1017/S1743921322004847 Published online by Cambridge University Press

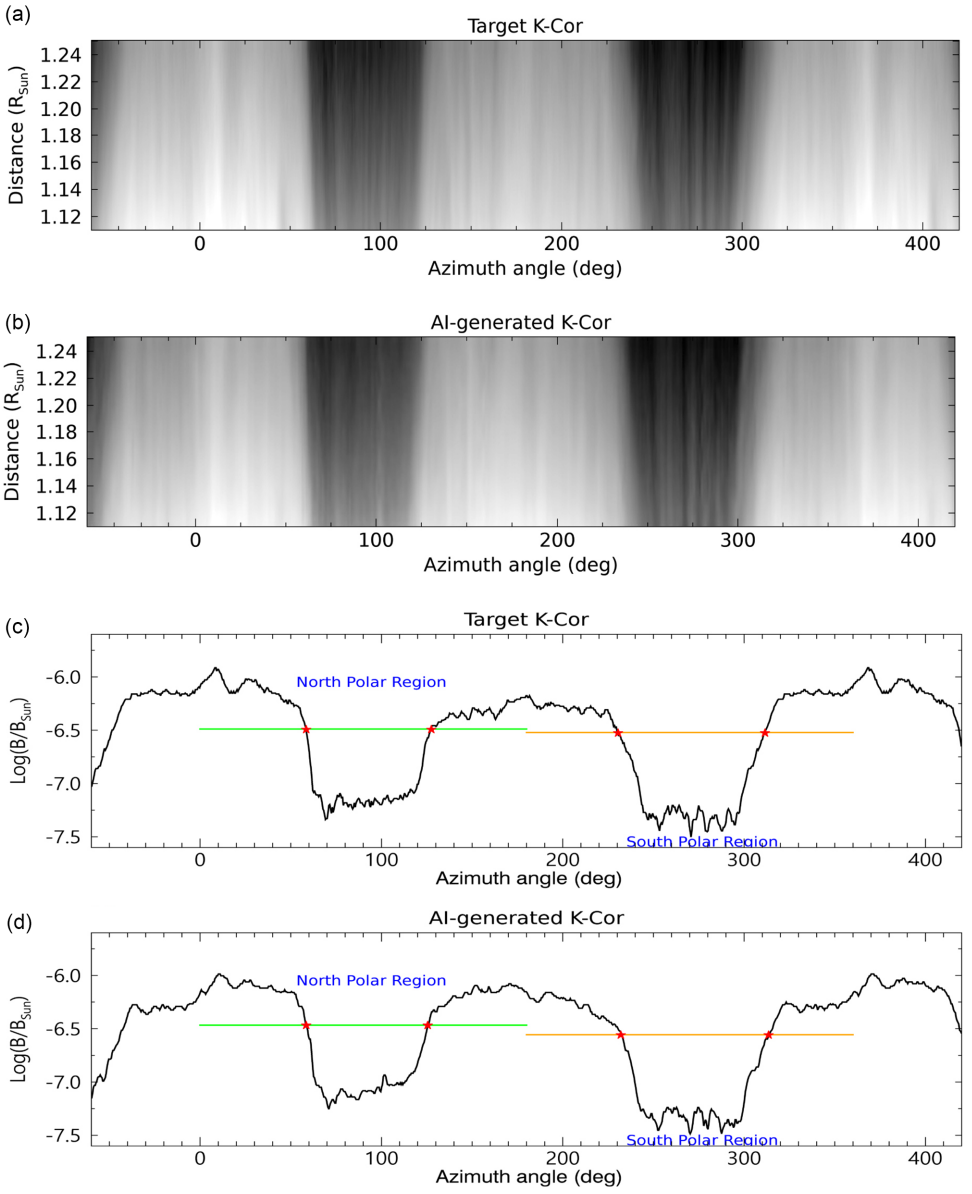

Figure 10. The white light images of the off-limb solar corona observed by K-Cor at 2018-Nov-27 19:38:52 UT (a) and its AI-generated image (b), corresponding intensity profiles averaged in the altitude range from 1.11 to 1.25 solar radii along azimuth angle (c, d). Green and orange lines are mean intensities of the northern and southern off-limbs, respectively (adapted from Lawrance et al. (2022)).

magnetograms (Park et al. 2020). This model is based on a deep convolutional generative adversarial network with a conditional loss for image-to-image translation from a single magnetogram (input) to a stacked magnetogram (target). For the input magnetogram, we use SDO/HMI line-of-sight magnetograms at solar disk center. For the target magnetogram, we make 21-frame-stacked magnetograms, taking into account solar rotation. We train the model using 7004 pairs of the input and target magnetograms from 2013 January to 2013 October. We then validate the model using 707 pairs from 2013 November and test the model using 736 pairs from 2013 December. Our major results

https://doi.org/10.1017/S1743921322004847 Published online by Cambridge University Press

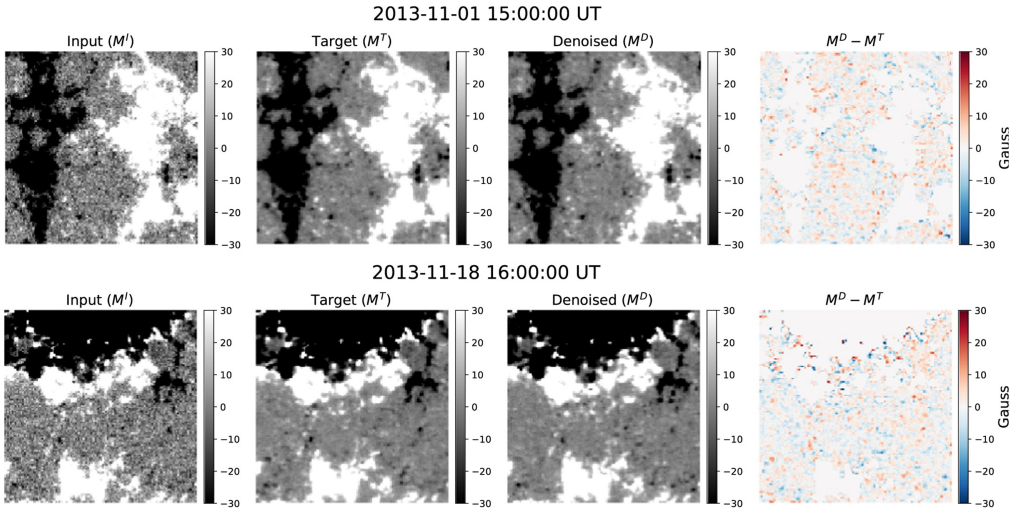

Figure 11. Two examples of comparisons of input, target, and de-noised magnetograms. The first column represents input magnetograms, the second column, target magnetograms, the third column, de-noised magnetograms from our model, and the last column, the difference maps between de-noised and target ones (adapted from Park et al. (2020)).

from this study are as follows. First, our model successfully denoises SDO/HMI magnetograms, and the de-noised magnetograms from our model are well consistent with the target ones (Figure 11). Second, the average noise level of the de-noised magnetograms is greatly reduced from 8.66 to 3.21 G, and it is consistent with that of the target magnetograms, 3.21 G. Third, the average pixel-to-pixel correlation coefficient value significantly increases from 0.88 (input) to 0.94 (de-noised), which means that the de-noised magnetograms are more consistent with the target ones than the input ones. Our results would be applied to many scientific fields in which the integration of many frames (or long-exposure observations) are used to increase the S/N.

2.9. *Improvement of IRI TEC maps*

We develop a DeepIRI model that generates by improving the total electron content (TEC) maps of the International Reference Ionosphere (IRI; Bilitza et al. 2017) model using DL based on conditional Generative Adversarial Networks (Ji et al. 2020). We use pairs of IRI TEC maps and International Global Navigation Satellite Systems (GNSS) Service (IGS; Kumar et al. 2015) TEC maps from 2001 to 2011 for training the model and compare IGS TEC and DeepIRI TEC maps from 2013 to 2017 for evaluating the model. The DeepIRI TEC maps generated from our model are more similar to the IGS TEC maps than IRI TEC maps, and in particular, ionospheric peak structures generate much more successfully in the DeepIRI TEC model than the IRI-2016 model (Figure 12). Comparing the average differences with the IGS TEC maps, the DeepIRI model significantly improves the IRI TEC at low-latitude regions around the equatorial anomaly. These results demonstrate the potential of the DeepIRI model based on deep learning to improve the global TEC prediction ability of the IRI model.

2.10. *Super-resolution of solar magnetograms*

Image super-resolution is a technique of enhancing the resolution of an image where a high-resolution (HR) image is reconstructed from a low-resolution (LR) image. We

https://doi.org/10.1017/S1743921322004847 Published online by Cambridge University Press

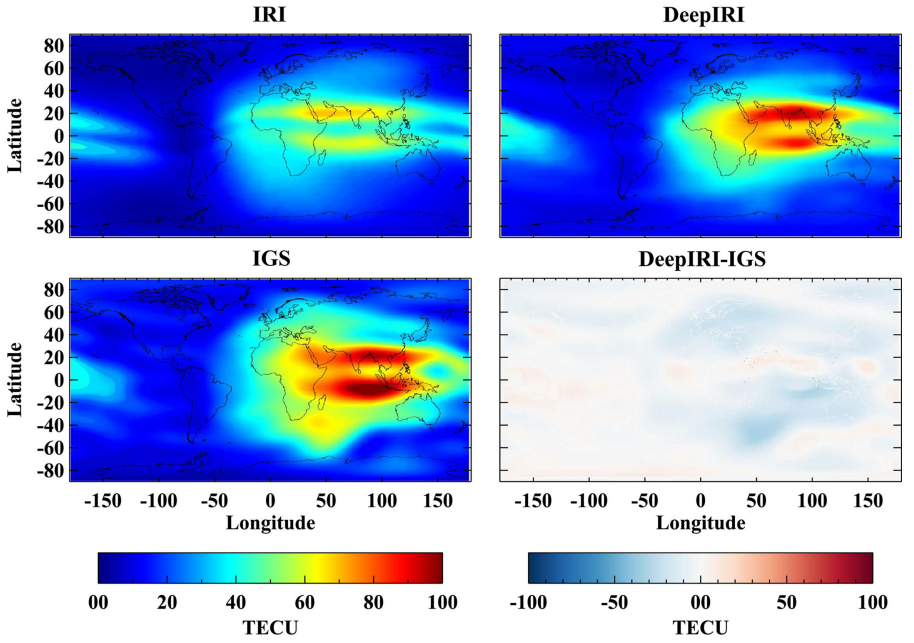

Figure 12. Example of the IRI TEC map, DeepIRI TEC map, IGS TEC map, and the difference map between the DeepIRI TEC and IGS TEC maps at 10 UT on 17 March 2015 (adapted from Ji et al. (2020)).

apply two novel DL models (residual attention model and progressive GAN model) to SDO/HMI magnetograms for super-resolution (Rahman et al. 2020). For this, we consider SDO/HMI0 magnetograms as output and their degraded ones with 4×4 binning as input. DL networks try to find internal relationships between LR and HR images from the given input and the corresponding output image. We use SDO/HMI magnetograms from 2014 May to August for training, from 2014 October to December for validation, and 2015 January to March for testing. We find that the DL models generate higher-quality results than the bicubic interpolation in terms of visual inspection and metrics (Figure 13). We apply this model to a full-resolution SDO/HMI magnetogram and then compare the generated magnetogram with the corresponding Hinode/SOT Narrowband Filtergrams (NFI) magnetogram. This comparison shows that the generated magnetogram is quite consistent with the Hinode one with a very good correlation (CC: 0.94) and a high similarity (SSIM: 0.93), which are better than the bicubic method.

3. Space Weather Forecast Based on Deep Learning

3.1. *Forecast of solar flare occurrence*

We apply CNN to the forecast of solar flare occurrence (Park et al. 2018). For this, we consider three CNN models (two pre-trained models, AlexNet and GoogLeNet, and one newly proposed model). Our inputs are the Solar and Heliospheric Observatory (SOHO; Domingo et al. 1995)/Michelson Doppler Imager (MDI; Scherrer et al. 1995) (from 1996 May to 2010 December) and SDO/HMI (from 2011 January to 2017 June) full-disk magnetograms at 00:00 UT. Model outputs are "Yes or No" of daily flare occurrence (C, M, and X classes) and they are compared with GOES flare identifications. We train the models using the input data and observations from 1996 to 2008, covering the entire solar cycle 23, and test them using the data sets from 2009 to 2017, covering solar cycle 24. Then we compare the results of our CNN models with those of three previous flare

https://doi.org/10.1017/S1743921322004847 Published online by Cambridge University Press

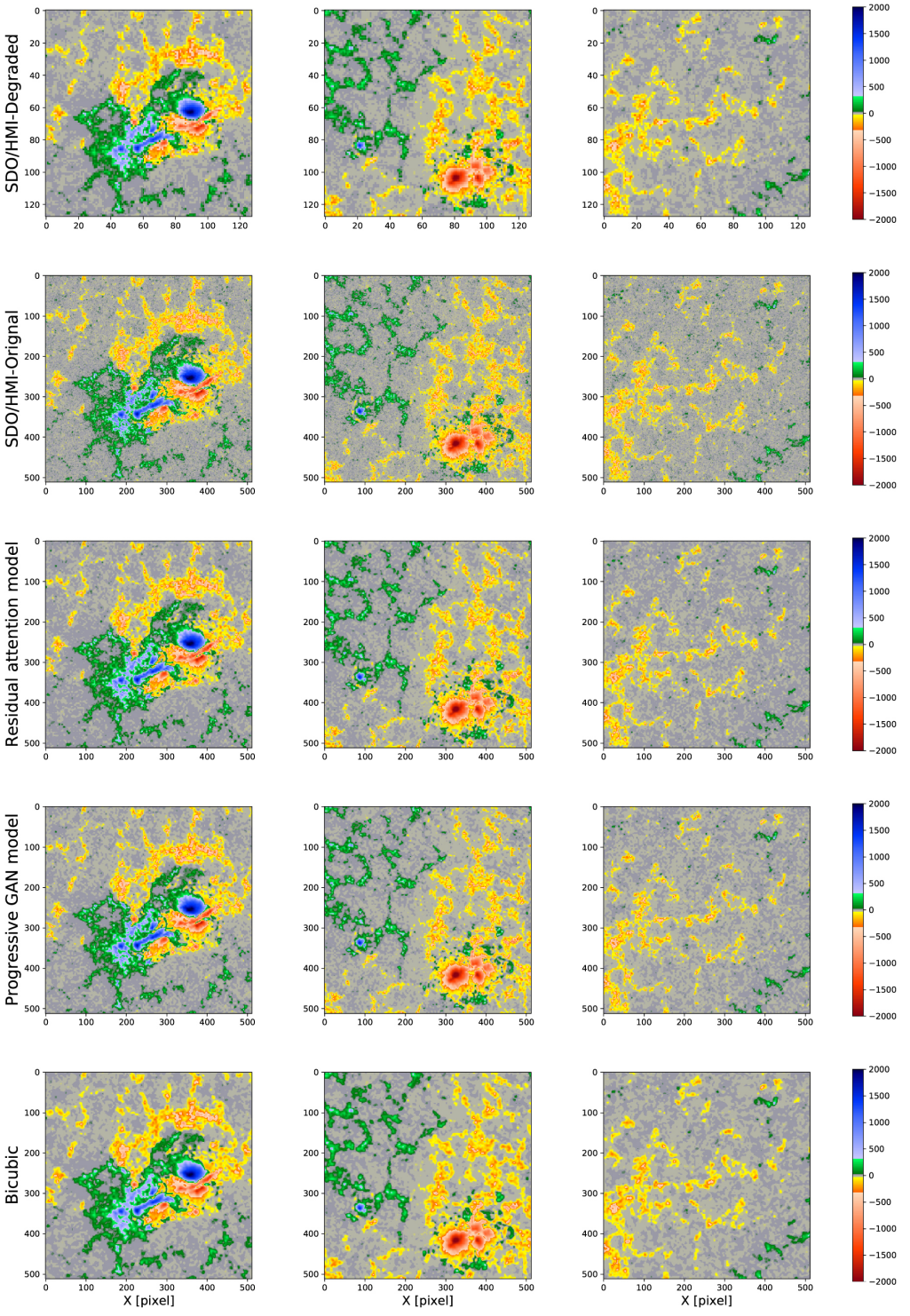

Figure 13. Results of DL models for super-resolution: input (first row), target (second row), AI-generated magnetograms (third and fourth row), and bicubic interpolation results (fifth row) for strong (first and second columns) and weak (third column) field regions. The target and input images are the original SDO/HMI magnetogram and its degraded low-resolution one, respectively (adapted from Rahman et al. (2020)).

https://doi.org/10.1017/S1743921322004847 Published online by Cambridge University Press

Table 1. The Results of our CNN Models and their comparison with three previous flare forecast models (adapted from Park et al. (2018)).

	This work			Colak & Qahwaji (2009)	Bloomfield et al. (2012)	Huang et al. (2018)
	Model 1	Model 2	Model 3			
ACC	0.78	0.79	0.82	0.81	0.71	0.76
POD	0.72	0.84	0.85	0.81	0.75	0.73
CSI	0.64	0.84	0.85	...	...	0.31
FAR	0.14	0.21	0.17	0.30	0.65	0.65
HSS	0.57	0.57	0.63	0.51	0.32	0.34
TSS	0.57	0.56	0.63	...	0.46	0.49
Data sets	Training: 1996-2008 Test: 2009-2017			Training: 1972-1998 Test: 1999-2002	Training: 1988-1996 Test: 1996-2010	Training: 1996-2010 Test: 2010-2015

forecast models in view of statistical scores. The major results from this study are as follows. First, we successfully apply CNN to the full-disk solar magnetograms without any preprocessing or feature extraction. Second, the results of our CNN models are considerably better in false alarm ratio (FAR) and critical success index than those of the previous solar flare forecasting models (Table 1). Third, our proposed model has better values of all statistical scores except for FAR, than the other two pre-trained models. Our results show a sufficient possibility that DL methods can improve the capability of not only the solar flare forecast but also similar types of forecast problems.

3.2. *Forecast of major solar X-ray flare flux profiles*

We make a DL model to forecast major solar flare X-ray flux profiles, based on a Seq2seq and an attention mechanism (Yi et al. 2020). The model forecasts 30 minutes of X-ray flux profiles. We train the model using 845 solar flare X-ray data from 1998 to 2006. The model performance is evaluated with RMSE. We compare the model with six other models based on deep learning methods and regression methods. The major results of this study are as follows. First, the model successfully forecasts solar flare X-ray flux profiles (Figure 13), without any preprocessing to extract features from data. Second, our proposed model achieves better performance than the other models. Third, our model shows lower RMSEs for low-peak fluxes flares than those with high-peak fluxes flares. Fourth, our model shows high CC for flare duration prediction.

3.3. *Visual explanation of a deep learning solar flare forecast model*

We make a new DL flare forecasting model to visually show the DL model explanation and compare them with the physical parameters of solar active regions (Yi et al. 2021). For this, we use full-disk magnetograms from 1996 to 2017. The model forecasts "Yes or No" of daily flare occurrence for C-, M-, and X-class. For model explanation, we use CNN attribution methods, guided backpropagation and Gradient-weighted Class Activation Mapping (Grad-CAM). The major results of this study are as follows. First, our DL model successfully forecasts daily solar flare occurrence with TSS = 0.65. Second, by the attribution methods, we find that the flare model importantly considers active regions (Figure 14) and the polarity inversion line. Third, Grad-CAM values of ARs and their flare occurrence rates of them are highly correlated. Fourth, Grad-CAM values are well correlated with nine SHARP parameters such as total unsigned vertical current, total unsigned current helicity, total unsigned flux, and total photospheric magnetic free energy density.

https://doi.org/10.1017/S1743921322004847 Published online by Cambridge University Press

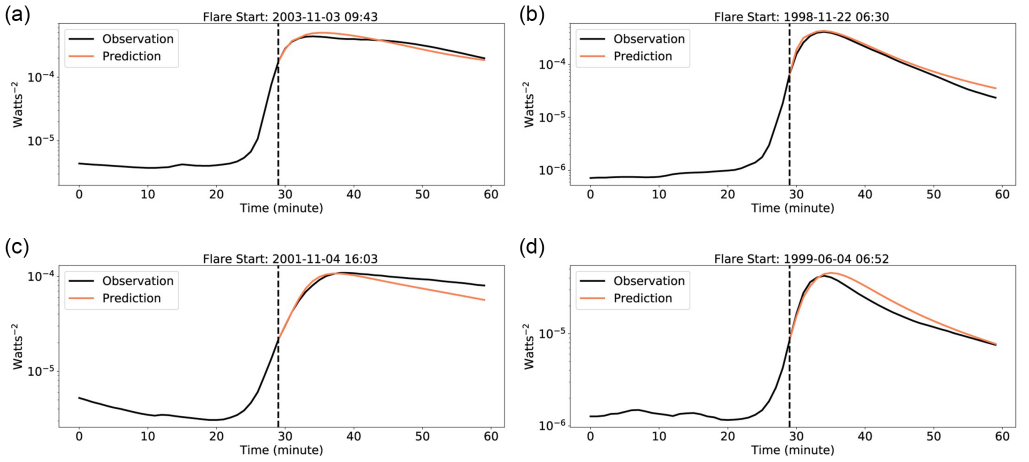

Figure 14. Solar flare X-ray forecasting results of X5 (a), X4 (b), X1 (c), and M4 (d) flare. (a), (b), (c), and (d) predictions are started 7, 7, 7, and 6 minutes after flare start time, respectively. The black vertical dashed lines denote forecast start times (adapted from Yi et al. (2020)).

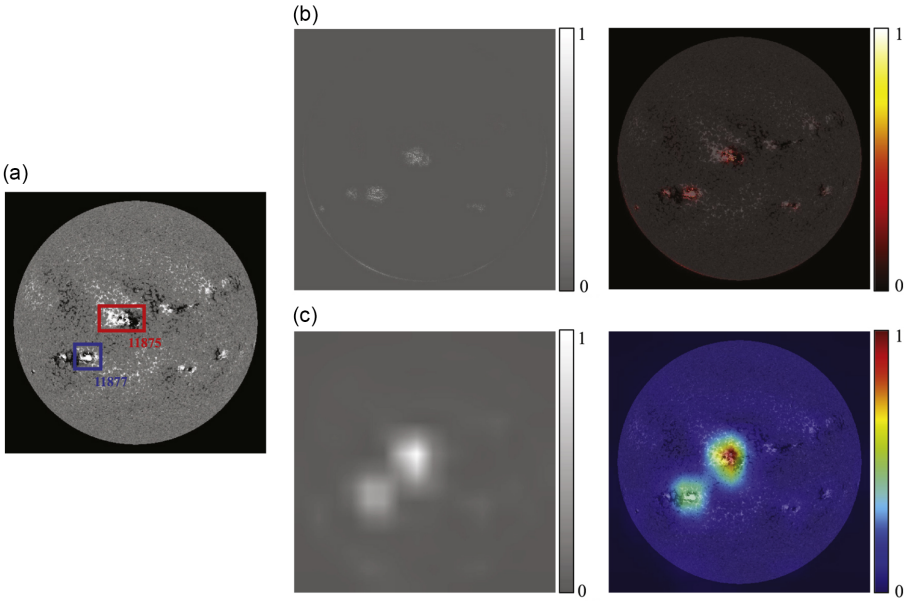

Figure 15. Results of attribution methods. (a) A line-of-sight magnetogram observed at 00:00 UT on 2013 October 23. (b) A guided backpropagation mask (left) and the mask overlaid on the magnetogram (right). (c) A Grad-CAM mask (left) and the mask overlaid on the magnetogram (right). The highlighted pixels/areas on masks indicate the gradient of pixels/areas for prediction (adapted from Yi et al. (2021)).

3.4. *Forecast of hourly relativistic (> 2 MeV) electron fluxes*

We forecast hourly relativistic (> 2 MeV) electron fluxes at geostationary orbit for the next 72 hours by using a multilayer perceptron based DL model (Son et al. 2022). The input data of our model are solar wind parameters: temperature, density, speed, interplanetary magnetic field (|B| and Bz), geomagnetic indices (Kp and Dst), and electron fluxes themselves. All input data are hourly averaged over the previous 72 hours. We obtain electron flux data from Geostationary Operational Environmental Satellite

https://doi.org/10.1017/S1743921322004847 Published online by Cambridge University Press

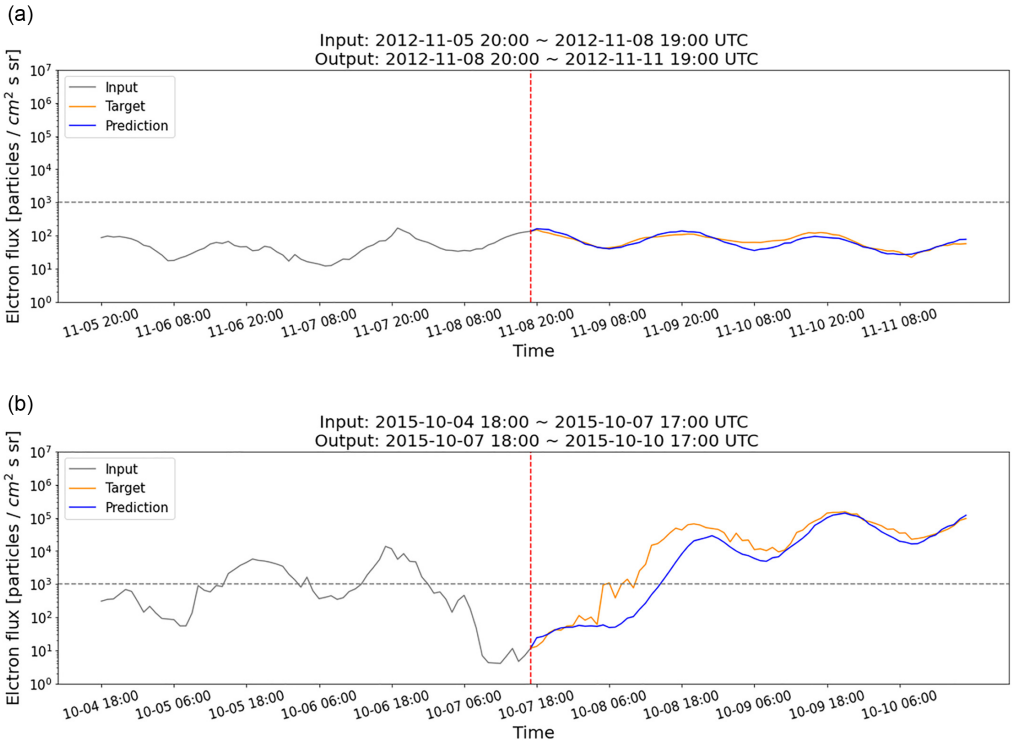

Figure 16. Two examples of our model results. Based on the red dashed line (prediction time), the left is the input time sequences and the right is the output time sequences. The gray lines are observed electron flux values during input time sequences, the yellow lines are target ones, and the blue lines are predicted ones by our model (adapted from Son et al. (2022)).

(GOES)-15 and -16, and perform the calibration for matching these two data. The total period of the data is from 2011 January to 2021 March (GOES-15 data for 2011–2017 and GOES-16 data for 2018–2021). We divide the dataset into a training set (January-August), a validation set (September), and a test set (October-December) to consider the solar cycle effect. Our major results are as follows. First, our model successfully predicts hourly electron fluxes for the next 72 hours (Figure 16). Second, prediction efficiency is from 0.97 (for 1 hr prediction) to 0.53 (for 72 hr prediction), and the root-mean-square error of our model is from 0.18 to 0.68, which are much better than those of the previous studies. Third, our model well predicts both diurnal variation and sudden changes in electron fluxes associated with fast solar winds and interplanetary magnetic fields. Our results demonstrate that the DL model can be applied to forecasting long-term sequential space weather events.

3.5. *Forecast of 1-day TEC maps*

We present a global TEC forecasting model using a novel DL method based on conditional generative adversarial networks (Yi et al. 2021). For training, we use the International GNSS Service (IGS) TEC maps from 2003 to 2012 with 2-hour time cadence. Our model has two input images (IGS TEC map and 1-day difference map between the present day and the previous day) and one output image (1-day future map). The model is tested with two different data sets: solar maximum period (2013–2014) and solar minimum period (2017–2018). Then, we compare the results of our model

https://doi.org/10.1017/S1743921322004847 Published online by Cambridge University Press

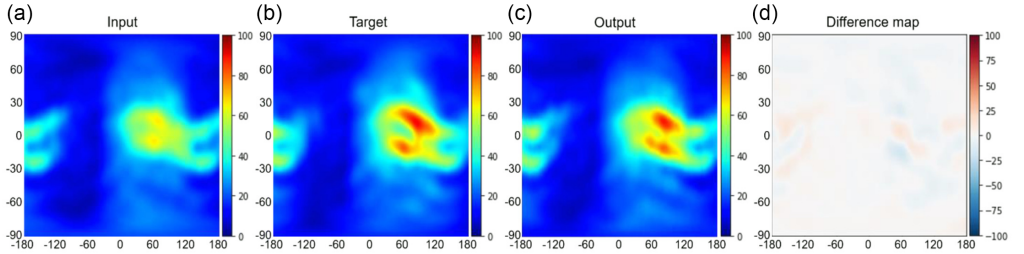

Figure 17. Comparison between IGS TEC maps and the results of our model at 02 UT on October 1, 2013. (a) input image, (b) target image (+24h IGS TEC), (c) output image generated by our model, (d) difference map (between [b and c]) (adapted from Lee et al. (2021b)).

with those of the 1-day CODE (Center for Orbit Determination in Europe, Schaer 1999) prediction model. Our major results can be summarized as follows. First, we successfully apply our model to the forecast of global TEC maps. Second, our model well predicts daily TEC maps with 1 day in advance using only previous TEC maps (Figure 17). The averaged root mean square error, bias, and standard deviation between AI-generated and IGS TEC maps are 2.74 TECU, -0.32 TECU, and 2.59 TECU, respectively. Third, our model generates some peak structures around equatorial regions. Fourth, our model shows better results than the 1-day CODE prediction model during both solar maximum and minimum periods. Fifth, another model with additional input data Kp index gives a slight improvement in the results. Our study demonstrates that our DL model based on an image translation method will be effective for forecasting future images using previous data.

4. Prospects

We have successfully applied novel DL methods to solar and space weather data. Especially, the task of image-to-image translation is quite promising and our new method (Pix2PixCC) is very useful for many scientific data. We are extending our applications to several cases: EUV images from historic Ca II ones, EUV images from coronal white light ones, H-alpha images from EUV ones, pixel-to-pixel translation among EUV images, fast construction of coronal physical parameters based on MAS, fast construction of coronal force-free fields, and three days forecast of global TEC maps.

In addition, the space weather applications by DL are underway in various aspects: application of reinforcement learning to solar flare forecast, construction of the ionospheric 3-D density model, automatic determination of CME parameters (like CDAW, Gopalswamy et al. 2009), automatic determination of CME 3-D parameters, and forecast of solar wind data, kp and Dst index using solar and interplanetary data. We have a plan to set up an integrated space weather model based on DL by combining the data from several different components: solar data, solar explosive events, solar wind, magnetosphere, and ionosphere/thermosphere.

Acknowledgements

We are very thankful to several teams for providing space-based and ground-based observation data: SOHO, SDO, STEREO, GOES, ACE, etc.

References

Bilitza, D., Altadill, D., Truhlik, V., et al. 2017, Space Weather, 15, 418

Bloomfield, D. S., Higgins, P. A., McAteer, R. T. J., & Gallagher, P. T. 2012, ApJ Letters, 747, L41

https://doi.org/10.1017/S1743921322004847 Published online by Cambridge University Press

Colak, T. & Qahwaji, R. 2009, Space Weather, 7, S06001
de Wijn, A. G., Burkepile, J. T., Tomczyk, S., et al. 2012, in Society of Photo-Optical Instrumentation Engineers (SPIE) Conference Series, Vol. 8444, Ground-based and Airborne Telescopes IV, ed. L. M. Stepp, R. Gilmozzi, & H. J. Hall, 84443N
Domingo, V., Fleck, B., & Poland, A. I. 1995, Solar Physics, 162, 1
Ermolli, I., Criscuoli, S., Centrone, M., Giorgi, F., & Penza, V. 2007, A&A, 465, 305
Ermolli, I., Fofi, M., Bernacchia, C., et al. 1998, Solar Physics, 177, 1
Galilei, G., Welser, M., & de Filiis, A. 1613, Istoria E dimostrazioni intorno alle macchie solari E loro accidenti comprese in tre lettere scritte all'illvstrissimo signor Marco Velseri ...
Gopalswamy, N., Yashiro, S., Michalek, G., et al. 2009, Earth Moon and Planets, 104, 295
Hochreiter, S. & Schmidhuber, J. 1997, Neural Comput., 9, 1735–1780
Huang, X., Wang, H., Xu, L., et al. 2018, ApJ, 856, 7
Isola, P., Zhu, J.-Y., Zhou, T., & Efros, A. A. 2017, in Proceedings of the IEEE Conference on Computer Vision and Pattern Recognition (CVPR)
Jeong, H.-J., Moon, Y.-J., Park, E., & Lee, H. 2020, ApJ Letters, 903, L25
Jeong, H.-J., Moon, Y.-J., Park, E., Lee, H., & Baek, J.-H. 2022, The Astrophysical Journal Supplement Series, 262, 50
Ji, E.-Y., Moon, Y.-J., & Park, E. 2020, Space Weather, 18, e02411
Kaiser, M. L., Kucera, T. A., Davila, J. M., et al. 2008, Space Science Reviews, 136, 5
Keller, C. U., Harvey, J. W., & Giampapa, M. S. 2003, in Innovative telescopes and instrumentation for solar astrophysics, Vol. 4853, International Society for Optics and Photonics, 194–204
Kim, T., Park, E., Lee, H., et al. 2019, Nature Astronomy, 3, 397
Kumar, S., Tan, E. L., & Murti, D. S. 2015, Earth, Planets and Space, 67, 42
Lawrance, B., Lee, H., Park, E., et al. 2022, ApJ, 937, 111
Lee, H., Park, E., & Moon, Y.-J. 2021a, ApJ, 907, 118
Lee, S., Ji, E.-Y., Moon, Y.-J., & Park, E. 2021b, Space Weather, 19, e2020SW002600
Lemen, J. R., Title, A. M., Akin, D. J., et al. 2012, Solar Physics, 275, 17
Lim, D., Moon, Y.-J., Park, E., & Lee, J.-Y. 2021, ApJ Letters, 915, L31
Mirza, M. & Osindero, S. 2014, arXiv preprint arXiv:1411.1784
Park, E., Moon, Y.-J., Lim, D., & Lee, H. 2020, ApJ Letters, 891, L4
Park, E., Moon, Y.-J., Shin, S., et al. 2018, ApJ, 869, 91
Pesnell, W. D., Thompson, B. J., & Chamberlin, P. C. 2012, Solar Physics, 275, 3
Rahman, S., Moon, Y.-J., Park, E., et al. 2020, ApJ Letters, 897, L32
Schaer, S. 1999, Geod.-Geophys. Arb. Schweiz, 59
Scherrer, P. H., Bogart, R. S., Bush, R. I., et al. 1995, Solar Physics, 162, 129
Schou, J., Scherrer, P. H., Bush, R. I., et al. 2012, Solar Physics, 275, 229
Selvaraju, R. R., Cogswell, M., Das, A., et al. 2017, in 2017 IEEE International Conference on Computer Vision (ICCV), 618–626
Shin, G., Moon, Y.-J., Park, E., et al. 2020, ApJ Letters, 895, L16
Son, J., Cha, J., Moon, Y.-J., et al. 2021, ApJ, 920, 101
Son, J., Moon, Y.-J., & Shin, S. 2022, Space Weather, 20, e2022SW003153
Springenberg, J. T., Dosovitskiy, A., Brox, T., & Riedmiller, M. 2014, Striving for Simplicity: The All Convolutional Net
Sutskever, I., Vinyals, O., & Le, Q. V. 2014, Sequence to Sequence Learning with Neural Networks
Wang, T.-C., Liu, M.-Y., Zhu, J.-Y., et al. 2018, in 2018 IEEE/CVF Conference on Computer Vision and Pattern Recognition, 8798–8807
Yi, K., Moon, Y.-J., Lim, D., Park, E., & Lee, H. 2021, ApJ, 910, 8
Yi, K., Moon, Y.-J., Shin, G., & Lim, D. 2020, ApJ Letters, 890, L5